Estimation of the Electron Temperature Profile in Tokamaks Using Analytical and Neural Network Models*

Shira Morosohk, Andres Pajares, and Eugenio Schuster

Abstract— Generating energy from nuclear fusion in a toka-mak may highly benefit from precise control of both kinetic and magnetic spatially-varying properties of the plasma (hot ionized gas where the fusion reactions take place). The spatial dependence of a plasma property, from the core to the edge of the plasma, is referred to as profile. Many control algorithms being developed require accurate, real-time knowledge of the plasma space-dependent state. However, many of the diagnostics used to measure the plasma state provide data that can be noisy or require significant post-processing. Within this context, an observer has been developed using an extended Kalman filtering approach for the electron temperature profile. The model employed by the observer uses a combination of analytical components and trained neural networks to generate as accurate of a prediction as possible while working within real-time calculation constraints. Such neural networks provide high accuracies, fast calculation times, and wide applicability. In addition, with only two diagnostic measurements at different spatial locations, the observer is able to estimate the entire electron temperature profile. Simulation results show that the observer can correctly estimate this profile despite significant discrepancies in the initial electron temperature profile and relatively high levels of noise. After its implementation in the plasma control system of the DIII-D tokamak, this observer may be able to provide valuable information on the electron temperature to a variety of present and future controllers.

I. INTRODUCTION

Nuclear fusion is the process by which two or more nuclei merge to form larger, different nuclei. As this occurs, a small amount of the nuclei rest mass is converted into energy, making nuclear fusion a potential mechanism for electricity generation. In practice, this process is extraordinarily difficult to control and sustain. An approach currently being studied is to use a tokamak [1] to contain the reaction fuels (deuterium and tritium, which are hydrogen isotopes). In order for two
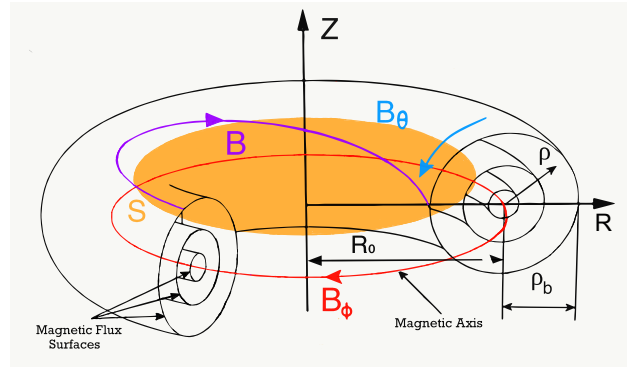
Fig. 1. Tokamak geometry showing the helical magnetic field B composed of toroidal field B_ϕ and poloidal field B_θ. Under certain assumptions, a single spatial coordinate ρ can be employed to describe the plasma geometry from the magnetic axis (at R_0) to the edge of the plasma (i.e. the last-closed magnetic-flux surface, at ρ_b).

nuclei to fuse, they need to have enough kinetic energy to overcome the Coulombic forces that make them repel each other. For hydrogen, this means that the particles need to have a temperature of about 100,000,000 degrees. Because hydrogen at that temperature is in a plasma state and responds to magnetic fields, tokamaks use powerful magnets to confine the plasma in a torus shape. The combination of toroidal (B_ϕ) and poloidal (B_θ) magnetic fields shown in Fig. 1 creates a helical total magnetic field B. The helicity of the field lines confines both positively and negatively charged particles (i.e. ions and electrons). This creates a separation between the edge of the confined plasma and the structure of the machine, protecting the plasma facing components from the extreme temperature of the plasma.

Significant efforts are underway to develop plasma scenarios that include fusion relevant core temperature, density, and confinement time and that remain magnetohydrodynamically (MHD) stable in steady state [2]. Control schemes that facilitate the access to and sustainment of these plasmas are being developed in parallel (e.g. [3]). In particular, profile control (i.e. the regulation of the spatial shape of plasma properties between $\rho = 0$ and $\rho = \rho_b$ as shown in Fig. 1 [4]) is a problem of high interest within the fusion community [5], [6] . For example, the shape of the temperature spatial profile is closely related with the achievement of plasma conditions conducive to fusion reactions. Sometimes, regions with high temperature gradients and reduced transport (the so-called transport barriers) are formed, and can be highly beneficial to increase the overall plasma confinement. However, it must be noted that profile control by means of feedback requires that an estimation of the corresponding profile be

available in real time. For example, magnetic profiles such as the safety factor, q (a measure of the helicity of B), can be obtained in real time from equilibrium reconstruction codes. On the other hand, several methods for measuring kinetic profiles (e.g. temperature and density) exist, such as Thomson scattering. Named for measuring laser light scattered by electrons, Thomson scattering samples electron density via scattered light amplitude and electron temperature via scattered light frequency [7]. Measurements are taken at a finite number of spatial locations or integrated over the whole spatial domain. In addition, due to the nature of these diagnostics, the measurement accuracy and precision are limited by noise, and in some cases are unreliable. Therefore, the reconstruction of the whole density and temperature profile from these measurements is computational intensive and usually performed off-line. While some solutions have been recently proposed for real-time processing of raw measurements, these solutions are usually based on data fitting by assuming a predefined shape of the profile and not on physics-based models.

In order to address these issues, state estimation techniques have been used to estimate both kinetic and magnetic profiles in tokamaks [8], [9]. Non-linear techniques, including extended Kalman filters and port-Hamiltonian observers, have been used to estimate a variety of profiles including the electron temperature, density, and poloidal flux. However, all of these observers rely on physics-based or empirical models as opposed to machine learning models. There has been very little research combining machine learning models with traditional observer design for plasma profile estimation. The combination of neural networks and machine learning-based models with more "traditional", analytical models may have several advantages. First, many physics-oriented models of plasma behavior, particularly kinetic behavior, are too computationally intensive to be useful in real-time applications. Because of this, control-oriented models are often used instead that may only be valid for specific plasma scenarios due to a limited number of tunable parameters. When trained of a sufficiently rich dataset, neural network models combine wider applicability to different plasmas scenarios with speed and accuracy. As a result, a number of machine learning models have been trained to replicate the results of computationally intensive physics-oriented codes [10]–[13]. In fact, machine learning has been used not only in fusion research, for example for disruption prediction (e.g. [14], [15]), but also in estimation applications outside the fusion community (e.g. [16]).

In this work, an observer is proposed to estimate the electron temperature (T_e) profile in real time. The nonlinear model used by this observer relies on neural networks to calculate the effects of neutral beam injection [11], which is used as a source of heat, current, and torque on the DIII-D tokamak, and the electron thermal diffusivity [12]. An extended Kalman filter, which is the nonlinear counterpart of the well-known Kalman filter for linear systems, is used to design the observer with the goal of rejecting internal and measurement noise while also retaining the nonlinearity of

the T_e dynamical model. The final objective of this estimator is to provide accurate, robust real-time state estimations of T_e which can be utilized by an electron temperature profile controller, as well as by any other controller, predictor, or supervisor that requires information about T_e.

The rest of the paper is organized as follows. In Section II, a model of the T_e profile evolution, including the two neural networks for the heating source and the electron thermal diffusivity, is introduced. In Section III, the extended Kalman filter (EKF) approach is described. Section IV shows simulation results of the observer. Conclusions and future work are discussed in Section V.

II. MODEL

The model used in this work takes the standard assumption of symmetry in the toroidal direction of the plasma. Under ideal MHD conditions [1], a single spatial coordinate that indexes flux surfaces (shown in Fig. 1) can be used to describe the plasma geometry. The 1-dimensional profiles are functions of time t and the spatial variable ρ (see Fig. 1). Known as the mean effective minor radius, the spatial variable ρ is defined as $\rho = \sqrt{\Phi/\pi B_{\phi,0}}$, where $\Phi \triangleq \int_{S_\phi} \vec{B}_\phi \cdot d\vec{S}_\phi$ is the toroidal magnetic flux, $B_{\phi,0}$ is the vacuum toroidal magnetic field at the geometric major radius R_0, and ρ_b is the mean effective minor radius of the last closed magnetic flux surface. Flux surfaces are defined by constant values of the poloidal stream function $\psi \triangleq \frac{1}{2\pi} \int_S \vec{B}_\theta \cdot d\vec{S}$ (see Fig. 1). The surface S has a boundary that is a toroidal ring and is normal to the z-axis. The normalized mean effective minor radius is defined as $\hat{\rho} = \rho/\rho_b$. Note the some profiles, including T_e, are not strictly functions of flux and therefore ρ; in these cases the values of these profiles are flux surface averages.

A. Electron Heat Transport Equation

The evolution of the $T_e(\hat{\rho}, t)$ profile in a tokamak can be described by a partial differential equation known as the electron heat transport equation,

$$\frac{3}{2} \frac{\partial}{\partial t}(n_e T_e) = \frac{1}{\rho_b^2 \hat{H}} \frac{1}{\hat{\rho}} \frac{\partial}{\partial \hat{\rho}} \left[\hat{\rho} \frac{\hat{G}\hat{H}^2}{\hat{F}} (\chi_e n_e) \frac{\partial T_e}{\partial \hat{\rho}} \right] + Q_e, \quad (1)$$

where $n_e(\hat{\rho}, t)$ is the electron density, $\chi_e(\hat{\rho}, t)$ is the electron thermal diffusivity, and $Q_e(\hat{\rho}, t)$ is the electron heating from a number of different sources. The quantities $\hat{F}(\hat{\rho})$, $\hat{G}(\hat{\rho})$, and $\hat{H}(\hat{\rho})$ are related to the magnetic configuration of a particular plasma equilibrium and in this model are assumed to be constant. The boundary conditions of (1) are given by

$$\left. \frac{\partial T_e}{\partial \hat{\rho}} \right|_{\hat{\rho}=0} = 0 \qquad T_e|_{\hat{\rho}_{ETB}} = T_{e,ETB}, \quad (2)$$

where $\hat{\rho}_{ETB}$ characterizes the location of the external transport barrier (ETB), or pedestal, found in H-mode plasmas [1]. Equation (1) gives the dynamics of T_e in the region $\hat{\rho} = [0, \hat{\rho}_{ETB}]$. Equation (1) is rewritten to separate the temporal and spatial derivatives of T_e as

$$\frac{\partial T_e}{\partial t} = f_1(\hat{\rho}, t) \frac{\partial^2 T_e}{\partial \hat{\rho}^2} + f_2(\hat{\rho}, t) \frac{\partial T_e}{\partial \hat{\rho}} + f_3(\hat{\rho}, t) T_e(\hat{\rho}, t) + f_4(\hat{\rho}, t), \quad (3)$$

where

$$f_1(\hat{\rho}, t) = \frac{2}{3} \frac{\hat{G}\hat{H}}{\rho_b^2 \hat{F}} \chi_e(\hat{\rho}, t), \tag{4}$$

$$f_2(\hat{\rho}, t) = \frac{2}{3} \frac{\hat{G}\hat{H}}{\rho_b^2 \hat{F}} \left[\frac{\chi_e(\hat{\rho}, t)}{n_e(\hat{\rho}, t)} \frac{\partial n_e}{\partial \hat{\rho}} + \frac{\partial \chi_e}{\partial \hat{\rho}} + \frac{\chi_e}{\hat{\rho}} \right]$$
$$+ \frac{\chi_e}{\rho_b^2 \hat{H}} \frac{\partial}{\partial \hat{\rho}} \left(\frac{\hat{G}\hat{H}^2}{\hat{F}} \right), \tag{5}$$

$$f_3(\hat{\rho}, t) = \frac{-1}{n_e(\hat{\rho}, t)} \frac{\partial n_e}{\partial t}, \quad f_4(\hat{\rho}, t) = \frac{2Q_e(\hat{\rho}, t)}{3n_e(\hat{\rho}, t)}. \tag{6}$$

The total electron heating is calculated as

$$Q_e(\hat{\rho}, t) = Q_{ohm}(\hat{\rho}, t) + Q_{ec}(\hat{\rho}, t) + Q_{nbi}(\hat{\rho}, t)$$
$$- Q_{ei}(\hat{\rho}, t) - Q_{rad}(\hat{\rho}, t), \tag{7}$$

where Q_{ohm} is the ohmic heating, Q_{ec} is the electron cyclotron heating, Q_{nbi} is the neutral beam heating, Q_{ei} is the heat exchange between electrons and ions through collisions, and Q_{rad} is the radiative heat loss. Models for n_e, Q_{ohm}, Q_{ec}, Q_{ei}, and Q_{rad} are given in Section II-B. Models for Q_{nbi} and χ_e are given in Section II-C.

B. Electron Density and Heating using Analytical Models

The electron density profile is assumed to have a constant shape given by a reference profile $n_e^{prof}(\hat{\rho})$. The line-averaged electron density $\bar{n}_e(t)$ is assumed to be a known quantity. The electron density is then calculated as $n_e(\hat{\rho}, t) = n_e^{prof}(\hat{\rho})\bar{n}_e(t)$.

As given by (7), the electron heating is a combination of five different components: ohmic heating, electron cyclotron radiofrequency heating, neutral beam heating, collisions between ions and electrons, and radiative heat loss. Ohmic heating is calculated as

$$Q_{ohm}(\hat{\rho}, t) = \eta(\hat{\rho}, t)j_{tor}(\hat{\rho}, t)^2, \tag{8}$$

where the resistivity is calculated by the Spitzer model as $\eta(\hat{\rho}, t) = \frac{k_{sp}(\hat{\rho})Z_{eff}}{T_e(\hat{\rho},t)^{3/2}}$. The profile k_{sp} is a constant profile of the model, and Z_{eff} is the mean effective charge of the plasma ions. The toroidal current density is calculated as $j_{tor}(\hat{\rho}, t) = -\frac{1}{\mu_0 \rho_b^2 R_0 \hat{H}} \frac{1}{\hat{\rho}} \frac{\partial}{\partial \hat{\rho}} \left(\hat{\rho} \hat{G}\hat{H} \frac{\partial \psi}{\partial \hat{\rho}} \right)$, where μ_0 is the vacuum permeability. The value of ψ is assumed to be known from diagnostics and/or equilibrium reconstruction techniques. A common method of injecting auxiliary power into a tokamak plasma is using radiofrequency waves that resonate with some specific plasma frequency. In the DIII-D tokamak, this is done using electron cyclotron resonance heating [17]. The electron cyclotron heating is calculated as

$$Q_{ec}(\hat{\rho}, t) = Q_{ec}^{prof}(\hat{\rho})P_{ec}(t), \tag{9}$$

where the reference profile $Q_{ec}^{prof}(\hat{\rho})$ is a constant of the model and the electron cyclotron power $P_{ec}(t)$ is assumed to be known. Heating of the electrons through collisions with ions is calculated as

$$Q_{ei}(\hat{\rho}, t) = \nu_e(\hat{\rho}, t)n_e(\hat{\rho}, t)(T_e(\hat{\rho}, t) - T_i(\hat{\rho}, t)), \tag{10}$$

where the electron-ion collisionality is calculated as $\nu_e = \frac{0.041 T_e(\hat{\rho},t)^{-3/2}n_e(\hat{\rho},t)}{A_{eff}}$. For low impurity deuterium plasmas,
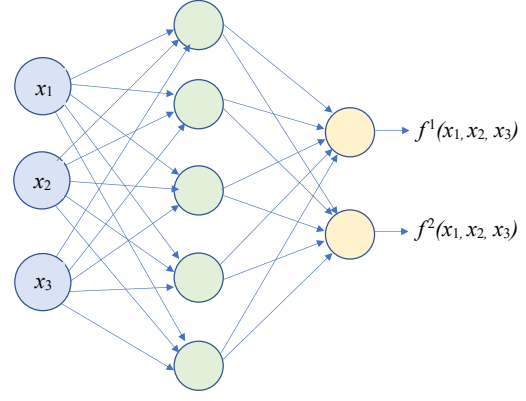

Fig. 2. Multi-layer perceptron neural network structure [12]. The network shown here has 3 inputs (x_1, x_2, and x_3), one hidden layer containing 5 neurons (in green), and 2 outputs (f^1 and f^2). The weights connecting each neuron in one layer to each neuron in the next layer, shown by the arrows, are learned through the training process.

the effective plasma mass A_{eff} is assumed to always be equal to 2. The ion temperature T_i used in Equation 10 is assumed to be a scalar multiple of T_e. For the radiation heat loss, only Bremsstrahlung [18] radiation is considered, so

$$Q_{rad}(\hat{\rho}, t) = k_b Z_{eff} n_e(\hat{\rho}, t)^2 \sqrt{T_e(\hat{\rho}, t)}, \tag{11}$$

where the Bremsstrahlung constant $k_b = 5.5 \times 10^{-37} \frac{Wm^3}{\sqrt{keV}}$.

C. Neural Networks

Two neural networks were developed in previous work [11], [12], and are used for the design of the T_e profile observer in this work. Both of them were trained to replicate the results of more complicated physics-oriented simulation codes that do not run fast enough to be used in real-time calculations. NubeamNet [11] was trained to replicate the Monte Carlo code NUBEAM [19], which predicts the effects of neutral beam injection on the plasma. Neutral beam injection involves injecting very fast atoms into the plasma which then ionize and transfer their energy to other particles through collisions, and is used as a source of heat, current, fuel, and torque. MMMnet [12] was trained to replicate the Multi-Mode Model (MMM) [20], which estimates turbulent diffusitivities, including the electron thermal diffusivity χ_e. Because electron heat transport is often dominated by turbulence in plasma scenarios of interest, χ_e as calculated by turbulent models like MMMnet plays a key role. Both neural networks use a simple multi-layer perceptron (MLP) structure (see Fig. 2), which only takes scalar inputs and outputs. Many of the inputs needed and outputs produced by these networks are 1-dimensional profiles. In order to be able to use an MLP, these profiles are reduced to a set of scalars using the principal component analysis technique.

D. Discretization using Finite Differences

1) In Space: The partial differential equation (3) is reduced to a system of ODEs using second order finite difference approximations for the spatial derivatives. The spatial grid is defined as $\Delta\hat{\rho} = \frac{1}{n}$, $\hat{\rho}_i = (i-1)\Delta\hat{\rho}$, $i \in \{1, ..., n\}$, over the range $\hat{\rho} \in [0, \hat{\rho}_{ETB}]$ where n is the number of spatial points, $\Delta\hat{\rho}$ is the distance between spatial
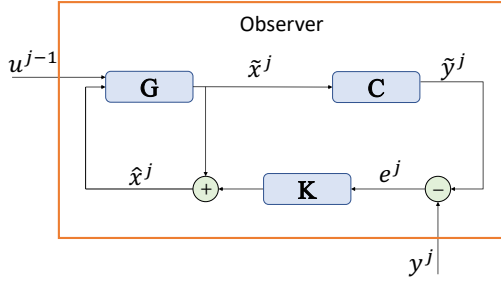
Fig. 3. Block diagram showing the prediction ($\tilde{x}^j$) and correction ($\hat{x}^j$) steps of the observer with K calculated by the extended Kalman filter.

points, and $\hat{\rho}_i$ represents the location of the ith spatial point. The notation $T_{e,i}$ is used to represent $T_e(\hat{\rho}_i, t)$. For $i \in [2, n-1]$, the system of ODEs is written as

$$\dot{T}_{e,i} = f_1(\hat{\rho}_i, t)\left(\frac{T_{e,i+1} + T_{e,i-1} - 2T_{e,i}}{\Delta\hat{\rho}^2}\right) \quad (12)$$

$$+ f_2(\hat{\rho}_i, t)\left(\frac{T_{e,i+1} - T_{e,i-1}}{2\Delta\hat{\rho}}\right) + f_3(\hat{\rho}_i, t)T_{e,i} + f_4(\hat{\rho}_i, t).$$

The state variable is initially defined as $x \triangleq \begin{bmatrix} T_{e,2} & T_{e,3} & \dots & T_{e,n-1} \end{bmatrix}^T$, and the input is defined as $u \triangleq \begin{bmatrix} \bar{n}_e & P_{ec} & P_{nbi1} & \dots & P_{nbi8} & I_p \end{bmatrix}^T$ where P_{nbi1-8} represent the powers from the eight neutral beams and I_p is the plasma current. Using these definitions of x and u, (12) can be written as

$$\dot{x} = g(x, u), \quad (13)$$

where g is a function defined by the right-hand side of (12).

2) In Time: The temporal grid is defined as $t^j = j\Delta t$, $j \in \{0, 1, ...\}$. The notation $T_{e,i}^j$ is used to represent $T_e(\hat{\rho}_i, t^j)$. A hybrid finite difference approach is used, with the functions f_1, f_2, f_3, and f_4 being evaluated at t^j and the T_e terms (other than the temporal derivative) being evaluated at t^{j+1}. This method preserves the unconditional stability of an implicit approach while keeping the calculation relatively simple and limiting the computation time. Equation (12) is then rewritten as

$$\frac{T_{e,i}^{j+1} - T_{e,i}^j}{\Delta t} = f_1(\hat{\rho}_i, t^j)\left(\frac{T_{e,i+1}^{j+1} + T_{e,i-1}^{j+1} - 2T_{e,i}^{j+1}}{\Delta\hat{\rho}^2}\right)$$

$$+ f_2(\hat{\rho}_i, t^j)\left(\frac{T_{e,i+1}^{j+1} - T_{e,i-1}^{j+1}}{2\Delta\hat{\rho}}\right) \quad (14)$$

$$+ f_3(\hat{\rho}_i, t^j)T_{e,i}^{j+1} + f_4(\hat{\rho}_i, t^j).$$

The state is now expanded to include the boundaries, so $x \triangleq \begin{bmatrix} T_{e,1} & T_{e,2} & \dots & T_{e,n} \end{bmatrix}^T$. The boundary condition at $\hat{\rho}_1 = 0$ from Eq. 2 is given by $4T_{e,2}^j - T_{e,3}^j - 3T_{e,1}^j = 0$. Instead of imposing a value of $T_{e,ETB}$, the boundary condition at $\hat{\rho}_n$ is assumed to be quasi-static, leading to $T_{e,n}^{j+1} = T_{e,n}^j$. Isolating the T_e^{j+1} terms, Equation (14) and the boundary conditions can be expressed as

$$x^{j+1} = G(x^j, u^j). \quad (15)$$

III. OBSERVER DESIGN

The model used by the observer is obtained from (15) as

$$x^{j+1} = G(x^j, u^j) + w^j \quad (16)$$

$$y^j = Cx^j + v^j. \quad (17)$$

The state equation (16) is equal to (15) with added internal noise w^j. In (17), C is a matrix of ones and zeros such that, when the added measurement noise $v^j = 0$, $y^j = [T_e(\hat{\rho}_{meas,1}, t^j) \ T_e(\hat{\rho}_{meas,2}, t^j)]^T$, where $\hat{\rho}_{meas,1}$ and $\hat{\rho}_{meas,2}$ are any two spatial locations where T_e is measured. The reason for using two measurements in this design is that this is the minimum value required for linear observability, as explained in Section IV-A. Internal and measurement noise are assumed to be uncorrelated Gaussian signals with zero mean and covariance matrices Q^j and R^j, respectively. The observer structure shown in Fig. 3 is used with the observer gain K calculated using an extended Kalman filter [21]. The prediction step of the extended Kalman filter is given by

$$\tilde{x}^j = G(\hat{x}^{j-1}, u^{j-1}) \quad (18)$$

$$\tilde{y}^j = C\tilde{x}^j \quad (19)$$

$$\tilde{P}^j = F^{j-1}\hat{P}^{j-1}F^{j-1^T} + Q^{j-1}, \quad (20)$$

where $\tilde{x}$, $\tilde{y}$, and $\tilde{P}$ represent the values of the state, outputs, and covariance of the state after the prediction step and $\hat{x}$ and $\hat{P}$ represent the values of the state and covariance of the state after the correction step. The matrix F is defined as the Jacobian of G, and in this work is calculated numerically using a first order finite difference formula. The correction step is given by

$$e^j = y^j - \tilde{y}^j \quad (21)$$

$$K^j = \tilde{P}^j H^{j^T}(H^j\tilde{P}^j H^{j^T} + R^j)^{-1}, \quad K_j \in \mathbb{R}^{n \times m} \quad (22)$$

$$\hat{x}^j = \tilde{x}^j + K^j e^j \quad (23)$$

$$\hat{P}^j = (I - K^j H^j)\tilde{P}^j, \quad (24)$$

where e is the error and K is the observer gain. In an EKF, H is defined as the Jacobian of the output equation (19); in this case, because the output equation is linear, the Jacobian H is simply equal to C.

IV. SIMULATION RESULTS

The observer has been tested in simulation to estimate T_e using simulated data from the Control Oriented Transport Simulator (COTSIM) code [5]. COTSIM evolves a number of 1D transport equations, including the electron heat transport equation (1) for T_e, as well as equations that describe the evolution of the safety factor and the rotation. COTSIM allows the user to choose from among a library of models, including neural network models, to calculate values such as the diffusivities and heat depositions. For this simulation, COTSIM is run using the experimental initial condition T_e^0 and inputs u from DIII-D shot 147634. This generates data that does not contain any noise; the noise vectors w^j and v^j are generated in the following manner and added to the COTSIM data at each time step. For the state noise, a matrix N_{int} is defined as

$$N_{int} = \begin{bmatrix} n & 0 & \dots & 0 \\ 0 & n-1 & \dots & 0 \\ 0 & 0 & \dots & 1 \end{bmatrix} \times N_{int,mag} \quad (25)$$
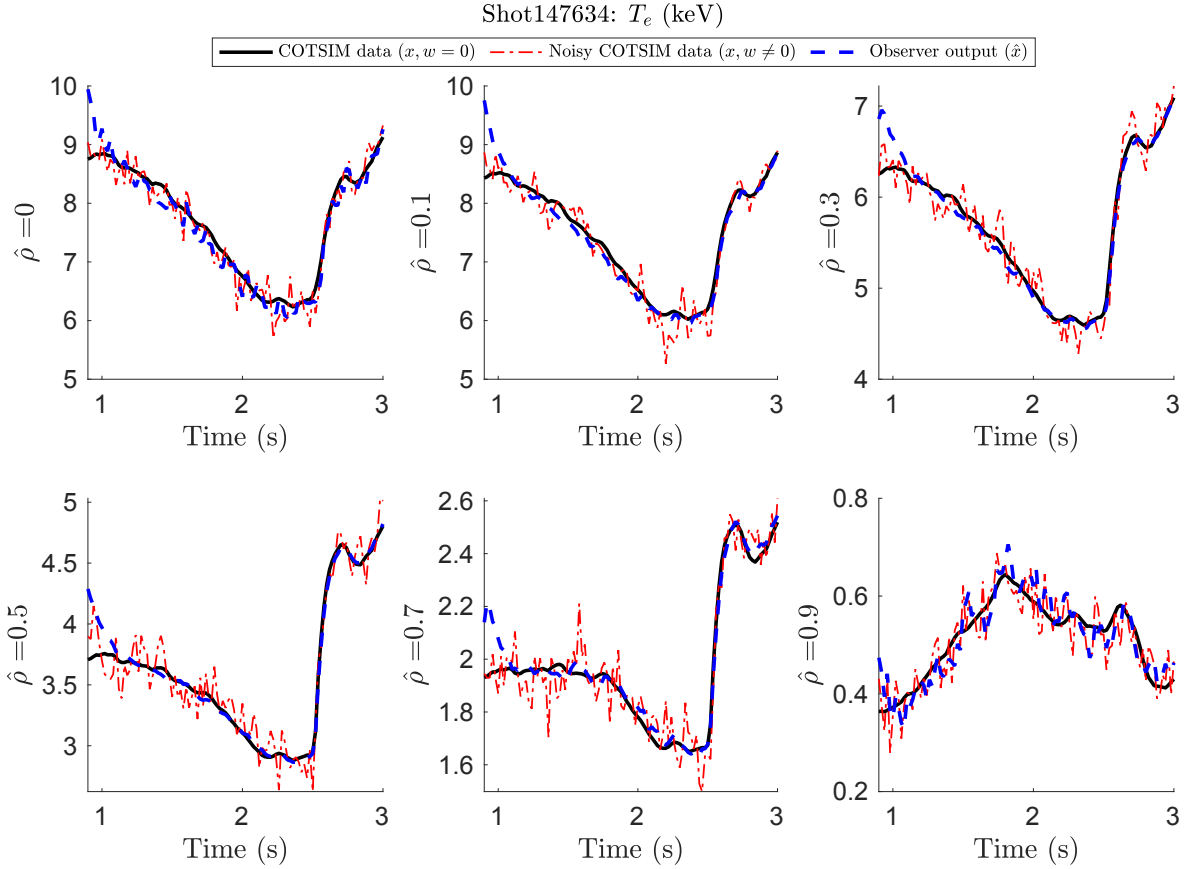
Fig. 4. Simulation of observer with added internal noise and measurement noise ($N_{int,mag} = 0.02$, $N_{meas,mag} = 0.05$), and a 10% over-prediction of the initial condition compared to COTSIM outputs plotted as a function of time.
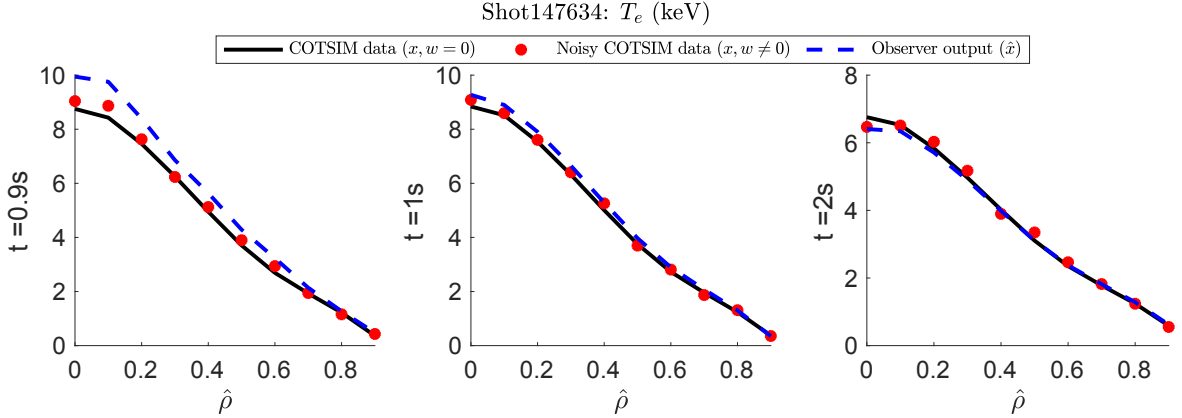

Fig. 5. Simulation of observer with added internal and measurement noise ($N_{int,mag} = 0.02$, $N_{meas,mag} = 0.05$), and a 10% over-prediction of the initial condition compared to COTSIM outputs plotted as a function of $\hat{\rho}$.

where $N_{int,mag}$ is a constant. The noise vector w^j added to the state for each time step of the COTSIM simulation is calculated as N_{int} multiplied by a vector of Gaussian white noise. In the simulations shown in this section and in most plasmas of interest, the temperature profile has a much higher magnitude at the center ($\hat{\rho} = 0$) than at the edge ($\hat{\rho} = \hat{\rho}_{ETB}$). Therefore, the structure of N_{int} in (25) was chosen to ensure that the magnitude of the added noise increases with the magnitude of the state at each spatial location. For the measurement noise, a matrix N_{meas} is

defined as

$$N_{meas} = \begin{bmatrix} n & 0 \\ 0 & 1 \end{bmatrix} \times N_{meas,mag} \qquad (26)$$

where $N_{meas,mag}$ is a constant. The noise vector v^j is calculated as N_{meas} multiplied by a vector of Gaussian white noise. The observer then assumes that the internal and measurement noise in the data have the following covariance matrices. The internal noise is assumed to have covariance matrix Q defined as $Q = N_{int}^T N_{int}$. The measurement noise is assumed to have covariance matrix R defined as $R = N_{meas}^T N_{meas}$.

A. Observability Analysis

While the state equation (16) is nonlinear, the use of the Jacobian F in the extended Kalman filter effectively linearizes the system at each time step. Because of this, the linear observability can be checked at each time step by calculating the observability matrix as $\begin{bmatrix} H & HF & HF^2 & \ldots & HF^{n-1} \end{bmatrix}^T$. Based on the simulations run, the output needs to include values of T_e measured at two different spatial locations in order for the system to be observable at every time step. Multiple different combinations of spatial locations can be used while maintaining linear observability.

B. Analysis of Simulation Results

Taking y as the T_e data simulated by COTSIM with the addition of the noise w_{sys}^j and v_{sys}^j, and u as the experimental inputs from DIII-D shot 147634, the observer was run to test its capabilities to estimate T_e while rejecting noise. The estimation case shown here begins at $t = 0.9s$ and assumes that $\hat{\rho}_{ETB} = 0.9$. The spatial locations $\hat{\rho}_{meas,1}$ and $\hat{\rho}_{meas,2}$ are chosen as 0 and 0.9, respectively, so $y = [T_{e,1}^j \ T_{e,n}^j]^T$. The simulation has a relatively high level of internal noise and a lower level of measurement noise added to the COTSIM data ($N_{int,mag} = 0.02$, $N_{meas,mag} = 0.001$). In addition, the observer in this simulation is given an initial condition that is 10% higher that the COTSIM data at that time. Figs. 4 and 5 show T_e as estimated by the observer for this simulation. Because the observer expects the level of noise that is seen in the data, it is able to reject noise at spatial locations across the whole T_e profile, as seen in Fig. 4. This figure also shows that the observer is able to correct the over-prediction arising from the different initial condition very quickly. This can also be seen in Fig. 5, where the initial condition given at 0.9s is clearly higher than the COTSIM data. The observer has almost entirely corrected this issue by 1s, and a nearly perfect match is seen at 2s.

V. CONCLUSIONS

A state observer has been developed to estimate the T_e profile in a tokamak. The nonlinear model is based on the electron heat transport equation, and includes a variety of control-oriented model components as well as two neural network versions of more computationally intensive physics-oriented codes. The model is fully observable with only two measured outputs, which reduces the need for real time processing of diagnostic data. The observer follows an extended Kalman filter approach, and has been shown to reject both errors in the initial condition and internal and measurement noise in simulation.

In order to obtain estimations across the whole range from $\hat{\rho} = 0$ to $\hat{\rho} = 1$, a pedestal model could be added to the observer model in future work. This may alter the observability requirements of the estimator. In addition, the observer validated on simulation data will be compared to real experimental data in the DIII-D tokamak both offline and in real time during experiments, and the two-point observability condition will be confirmed. Once the observer is validated in real time, the outputs can be used by a variety of controllers to aid in many different plasma control objectives.

REFERENCES

[1] J. Wesson, *Tokamaks*. Oxford, UK: Clarendon Press, 1984.

[2] R. Buttery, B. Covele, J. Ferron *et al.*, "DIII-D research to prepare for steady state advanced tokamak power plants," *Journal of Fusion Energy*, vol. 38, pp. 72–111, 2019.

[3] W. Wehner, M. Lauret, E. Schuster *et al.*, "Predictive control of the tokamak q profile to facilitate reproducibility of high-q_{min} steady-state scenarios at DIII-D," in *2016 IEEE Conference on Control Applications (CCA)*, 2016, pp. 629–634.

[4] M. L. Walker, P. De Vries, F. Felici, and E. Schuster, "Introduction to tokamak plasma control," in *2020 American Control Conference (ACC)*, 2020, pp. 2901–2918.

[5] A. Pajares and E. Schuster, "Current profile and normalized beta control via feedback linearization and Lyapunov techniques," *Nuclear Fusion*, vol. 61, no. 3, p. 036006, jan 2021.

[6] M. Boyer, K. Erickson, B. Grierson *et al.*, "Feedback control of stored energy and rotation with variables beam energy and perveance on DIII-D," *Nuclear Fusion*, vol. 59, 2019.

[7] K. Middaugh, B. Bray, C. Hsieh, B. McHarg, and B. Penaflor, "DIII-D Thomson scattering diagnostic data acquisition, processing, and analysis software," in *1999 IEEE Conference on Real-Time Computer Applications in Nuclear Particle and Plasma Physics. 11th IEEE NPSS Real Time Conference. Conference Record (Cat. No.99EX295)*, 1999, pp. 342–345.

[8] T. Blanken, F. Felici, C. Rapson, M. de Baar, and W. Heemels, "Control-oriented modeling of the plasma particle density in tokamaks and application to real-time density profile reconstruction," *Fusion Engineering and Design*, vol. 126, pp. 87–103, 2018.

[9] H. Wang, J. E. Barton, and E. Schuster, "Poloidal flux profile reconstruction from pointwise measurements via extended Kalman filtering in the DIII-D tokamak," in *2015 IEEE Conference on Control Applications (CCA)*, 2015, pp. 1309–1314.

[10] M. Boyer, S. Kaye, and K. Erickson, "Real-time capable modeling of neutral beam injection on NSTX-U using neural networks," *Nuclear Fusion*, vol. 59, no. 056008, 2019.

[11] S. M. Morosohk, M. D. Boyer, and E. Schuster, "Accelerated version of NUBEAM capabilities in DIII-D using neural networks," *Fusion Engineering and Design*, vol. 163, p. 112125, 2021.

[12] S. M. Morosohk, A. Pajares, T. Rafiq, and E. Schuster, "Neural network model of the multi-mode anomalous transport module for accelerated transport simulations," *Nuclear Fusion*, vol. 61, p. 106040, 2021, in press.

[13] O. Meneghini, S. Smith, P. Snyder *et al.*, "Self-consistent core-pedestal transport simulations with neural network accelerated models," *Nuclear Fusion*, vol. 57, no. 086034, 2017.

[14] C. Rea, K. J. Montes, K. G. Erickson, R. S. Granetz, and R. A. Tinguely, "A real-time machine learning-based disruption predictor in DIII-D," *Nuclear Fusion*, vol. 59, no. 9, p. 096016, 2019.

[15] Y. Fu, D. Eldon, K. Erickson *et al.*, "Machine learning control for disruption and tearing mode avoidance," *Physics of Plasmas*, vol. 27, p. 022501, 2020.

[16] A. Lakhal, A. Tlili, N. Braiek *et al.*, "Neural network observer for nonlinear systems application to induction motors 1," *International Journal of Control and Automation*, vol. 3, 04 2010.

[17] E. Ott, B. Hui, and K. Chu, "Theory of electron cyclotron resonance heating of tokamak plasmas," *Physics of Fluids*, vol. 23, p. 1031, 1980.

[18] D. Post, J. Abdallah, R. Clark, and N. Putninskaya, "Calculations of energy losses due to atomic processes in tokamaks with applications to the international thermonuclear experimental reactor divertor," *Physics of Plasmas*, vol. 2, p. 2328, 1995.

[19] R. Goldston, D. McCune, H. Towner, S. Davis, R. Hawryluk, and G. Schmidt, "New techniques for calculating heat and particle source rates due to neutral beam injection in axisymmetric tokamaks," *Journal of Computational Physics*, vol. 43, pp. 61–78, 1981.

[20] T. Rafiq, A. Kritz, J.Weiland, A. Pankin, and L. Luo, "Physics basis of multi-model anomalous transport module," *Physics of Plasmas*, vol. 20, p. 032506, 2013.

[21] B. D. O. Anderson and J. B. Moore, *Optimal Filtering*. Englewood Cliffs, NJ: Prentice-Hall, 1979.